Science Advances

AAAS

advances.sciencemag.org/cgi/content/full/3/10/e1701084/DC1

Supplementary Materials for

Ultrathin thermoresponsive self-folding 3D graphene

Weinan Xu, Zhao Qin, Chun-Teh Chen, Hye Rin Kwag, Qinli Ma,
Anjishnu Sarkar, Markus J. Buehler, David H. Gracias

Published 6 October 2017, *Sci. Adv.* **3**, e1701084 (2017)
DOI: 10.1126/sciadv.1701084

This PDF file includes:

- Additional experimental details
- Raman spectra of the functionalized graphene
- AFM characterization of the functionalized graphene
- XPS characterization of functionalized graphene
- Optical and SEM imaging of the self-folding graphene structures
- Raman spectra of folded graphene
- Cell encapsulation and Raman analysis
- Full atomistic modeling of the folding behaviors
- Electrical properties of folded graphene structures
- fig. S1. Raman spectra of PD with different thickness (self-polymerization for 2 and 4 hours) on the Si substrate.
- fig. S2. Surface morphology of graphene and functionalized graphene.
- fig. S3. Chemical composition of functionalized graphene studied by XPS.
- fig. S4. High-resolution O1s XPS spectra and peak fitting (dotted lines) of graphene, G-PD, and G-PD-PNIPAM.
- fig. S5. Effect of the rigid hinge on the self-folding of functionalized graphene box.
- fig. S6. Characterization of the self-folding graphene microstructures using SEM.
- fig. S7. Highly parallel self-folding of ultrathin 3D graphene microstructures.
- fig. S8. Control experiments of self-folding on pristine graphene and G-PD.
- fig. S9. Self-folding of functionalized graphene with 5 nm thickness.
- fig. S10. The folding process of half-functionalized graphene dumbbell with increasing temperature.
- fig. S11. Raman spectra of a graphene flower in the flat and folded regions.
- fig. S12. Cell viability with the live/dead assay.

- fig. S13. Single cell encapsulation and Raman study.
- fig. S14. Initial configuration of the PNIPAM-water system in the MD model.
- fig. S15. Top view of the aggregation behavior of an array of (36 chains in total) PNIPAM brushes at different temperatures in MD simulations.
- fig. S16. Comparison between the coarse-grained MD model and the experiment results for a functionalized graphene flower with different size.
- fig. S17. The effect of mechanical properties of the two layers on self-folding.
- fig. S18. Electrical measurements on pristine graphene and functionalized graphene dumbbell.
- fig. S19. Dimension of the folding crease measured by AFM.
- fig. S20. Output and transfer curves of the pristine and functionalized graphene FET.
- table S1. XPS data analysis of graphene, G-PD, and G-PD-PNIPAM at the C1s, N1s, and O1s peaks.
- table S2. Tensile test results of PNIPAM from the MD simulations.

1. Additional experimental details

1.1. Preparation of the patterned Al/Si substrate and graphene transfer

The substrates used in all our experiments were composed of a silicon (Si) wafer with a thermally grown 300 nm thick oxide (SiO_2) film. In order to enable the selective attachment of graphene to the substrate *via* van der Waals forces, a patterned Al layer was deposited on top of the SiO_2 using lift-off metallization. Briefly, the SiO_2/Si wafer was first patterned by photolithography, leaving a patterned layer of photoresist (SC 1827 MicroChem) on the surface. Then a thin layer of Al (40 nm) was thermally evaporated on the surface. The photoresist was dissolved in acetone, leaving behind a patterned layer of Al on the SiO_2/Si wafer.

CVD monolayer graphene was purchased from Graphene Supermarket (Reading, MA, USA), and was transferred onto the patterned substrates using the PMMA transfer method. Briefly, a layer of PMMA (Sigma Aldrich, M_w: 996,000) was spin coated on the graphene, and after thermal annealing, graphene on the other side of the copper foil was removed using an oxygen plasma. Then, the graphene/PMMA film on the copper foil was placed into an aqueous iron chloride ($FeCl_3$) solution (1 mol/L) to etch away the copper. The PMMA/graphene films were washed with deionized water (twice) followed by hydrochloric acid (10%) and then deionized water (thrice) to remove any residual ions. Subsequently, the graphene/PMMA films were transferred onto the patterned substrate, and the PMMA layer was dissolved by immersion in acetone for 6 h.

1.2. Cell culture and encapsulation

The breast cancer cell line MDA-MB-231 (ATCC, Manassas, VA, USA) was used in this work. Cells were grown in DMEM media supplemented with 10% fetal bovine serum (FBS) and 1% penicillin-streptomycin in a humidified incubator at 37 ^oC and 5% CO_2. The live/dead assay was performed by incubating the cells with calcein AM and ethidium homodimer-1 (Thermo Fisher Scientific, Rochester, NY, USA) in PBS solution at 37 ^oC for 30 min. The cells were then examined under a confocal microscope (Zeiss LSM 510).

For the encapsulation of cells with graphene, the cells were trypsinized and suspended in fresh culture media. Then a certain amount of the cell suspension was added to a Petri dish which contains the substrate with functionalized graphene microstructures on it. The elevated temperature during cell culture (37 ^oC) induces the folding of the functionalized graphene structures, which can encapsulate the cells inside.

2. Raman spectra of the functionalized graphene

After surface functionalization with PD and PNIPAM, peaks at 1350 and 1591 cm^{-1} broaden, which can be attributed to the presence of PD. The intensity of these peaks increases with increasing PD functionalization time suggesting formation of a thicker film. The reference spectra of PD with two different thickness on a bare silicon substrate is shown in fig. S1. PNIPAM does not show a measurable Raman signal in comparison to the signal of PD and graphene at the wavenumber range studied.

PD itself exhibits two broad weak peaks at 1350 and 1580 cm^{-1} in Raman (fig. S1), which correspond to the stretching and deformation of the aromatic rings. After depositing PD on the surface of graphene, it can be seen that there is an increase in the D band intensity. Based on the overlapping peaks with PD, we believe that this increase is due to PD and not due to defects in graphene. The shape and intensity of the G band changes after PD deposition: pristine graphene has a sharp peak, while for G-PD the bottom part of the peak becomes broader; there is also a small increase in G band intensity. Such effects become more significant with an increase of PD layer thickness, as can be seen from Raman of G-PD2 and G-PD4 (dopamine polymerization for 2 hours and 4 hours, respectively).

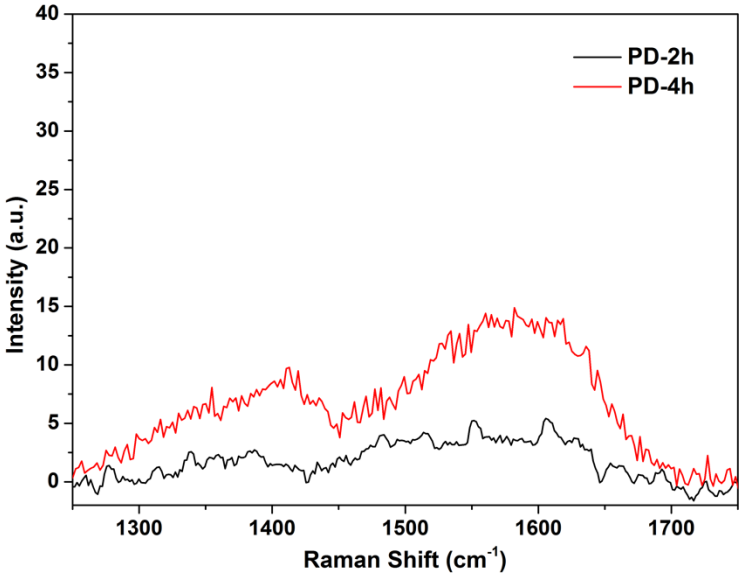

fig. S1. Raman spectra of PD with different thickness (self-polymerization for 2 and 4 hours) on the Si substrate.

3. AFM characterization of the functionalized graphene

The thickness and surface morphology of the functionalized graphene were studied by atomic force microscopy (AFM) (fig. S2). The line scans indicate that the pristine graphene on the Si substrate has a thickness of 0.8 nm, and after PD deposition, the thickness increases to 6.0 and 6.9 nm for G-PD2 and G-PD4, respectively. The surface of G-PD is smooth and uniform, which indicates the strong and intimate interaction between PD and graphene. After further grafting of PNIPAM, the thickness of the G-PD-PNIPAM further increases to 8.5, 8.9 and 9.6 nm for grafting reaction of 12h, 18h, and 24h.

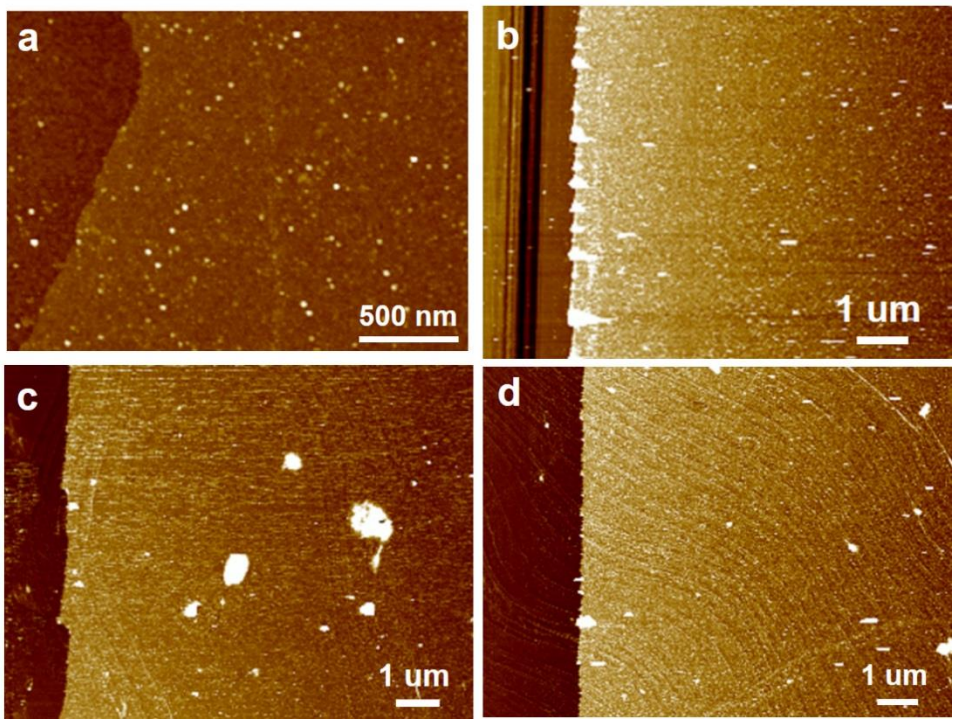

fig. S2. Surface morphology of graphene and functionalized graphene. AFM images of pristine graphene (**a**). G-PD4 (**b**), G-PD2-PNIPAM12 (**c**), and G-PD2-PNIPAM24 (**d**). Z range is 20 nm.

4. XPS characterization of functionalized graphene

The chemical composition of the functionalized graphene was characterized by X-ray Photoelectron Spectroscopy (XPS). Fig. S3 shows the XPS survey spectra for graphene, G-PD, and G-PD-PNIPAM, which were collected over the binding energy (B.E.) range from 0 to 1100 eV with a step size of 1 eV. It can be seen that the C1s and O1s peak exist for all three samples, G-PD and G-PD-PNIPAM have an additional N1s peak, while pure graphene does not, and the N1s peak intensity is stronger for G-PD-PNIPAM, which proves the successful deposition of PD and subsequent grafting of PNIPAM on the surface of graphene.

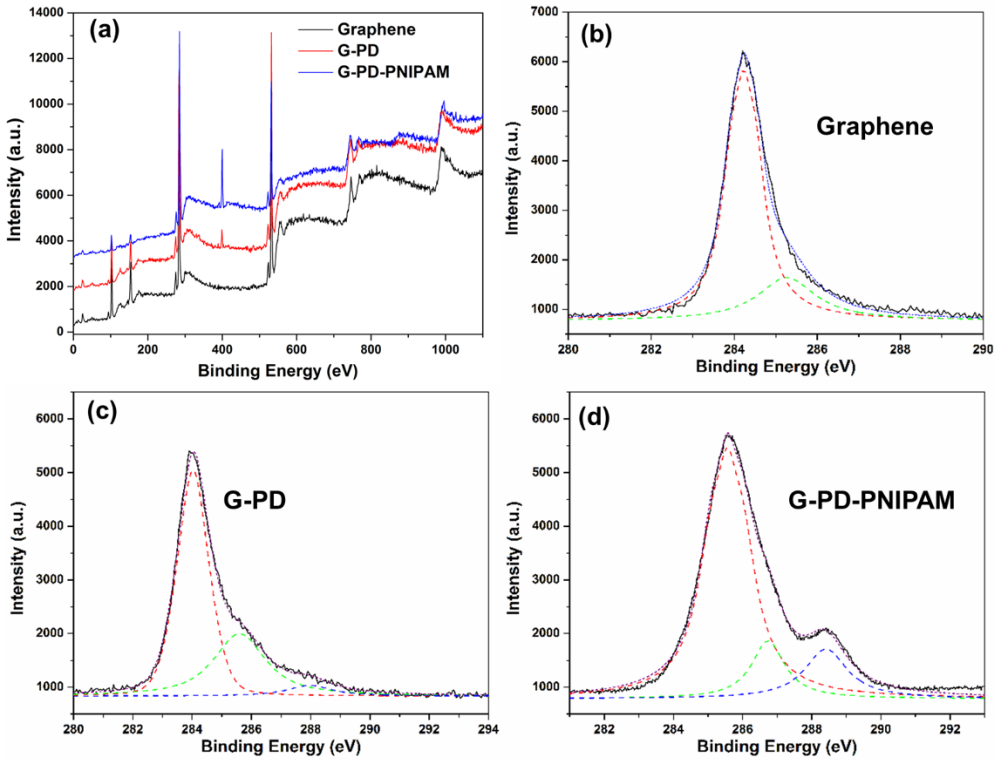

fig. S3. Chemical composition of functionalized graphene studied by XPS. (**a**) XPS spectra of graphene and functionalized graphene on SiO_2/Si substrate. High resolution C1s XPS spectrum and peak fitting of (**b**) graphene, (**c**), G-PD, and (**d**) G-PD-PNIPAM.

For the graphene sample, the C1s peak can be decomposed into two apparent spectral components at 284.2 and 285.3 eV (fig. S3b), the main peak at 284.2 eV corresponds to the graphite-like sp^2 carbon, and the small peak at 285.3 eV is the sp^3 carbon from defects and edge of the graphene, and the energy difference between sp^2 and sp^3 carbon atoms is 0.9 eV. The C1s peak for G-PD can be deconvoluted into three component (fig. S3c): sp^2 C-H on the aromatic rings at 284.0 eV, which is the major one; C-O/ C-N species at 285.6 eV, and C=O/C=N species at 287.9 eV (table S1). After PNIPAM grafting, the C1s peak has an obvious change in shape and position, it can be decomposed into three peaks, the major one at

285.6 eV for CH_x, another one at 286.7 eV for C-C=O groups, and a third one at 288.4 eV for N-C=O groups.

table S1. XPS data analysis of graphene, G-PD, and G-PD-PNIPAM at the C1s, N1s, and O1s peaks.

Sample	C1s			N1s			O1s		
	group	BE (eV)	percent	group	BE (eV)	percent	group	BE (eV)	percent
Graphene	sp^2 C	284.2	78.7%						
	sp^3 C	285.3	21.3%						
G-PD	CH_x (sp^2)	284.0	62.9%	R-NH_2	399.5	88.2%	O=C	532.7	92.8%
	C-O / C-N	285.6	32.2%	R_2-NH	400.5	11.8%	O-C	531.1	7.2%
	C=O / C=N	287.9	4.9%						
G-PD-PNIPAM	CH_x (sp^3)	285.6	72.3%	R_2-NH	400.5	100%	O=C	532.4	100%
	C-C=O	286.7	13.3%						
	N-C=O	288.4	14.4%						

The O1s peak (fig. S4) exists for graphene sample, which comes from the SiO_2 substrate underneath, and the peak can be fitted with a single peak at 532.9 eV (SiO_2). For G-PD, the O1s region is fit with two peaks assigned to O=C and O−C species, which are located at 532.7 and 531.1 eV, respectively (table S1), with the former being the majority. For G-PD-PNIPAM, with the grafting of PNIPAM, there is only one peak at 532.4 eV, which corresponds to O=C groups.

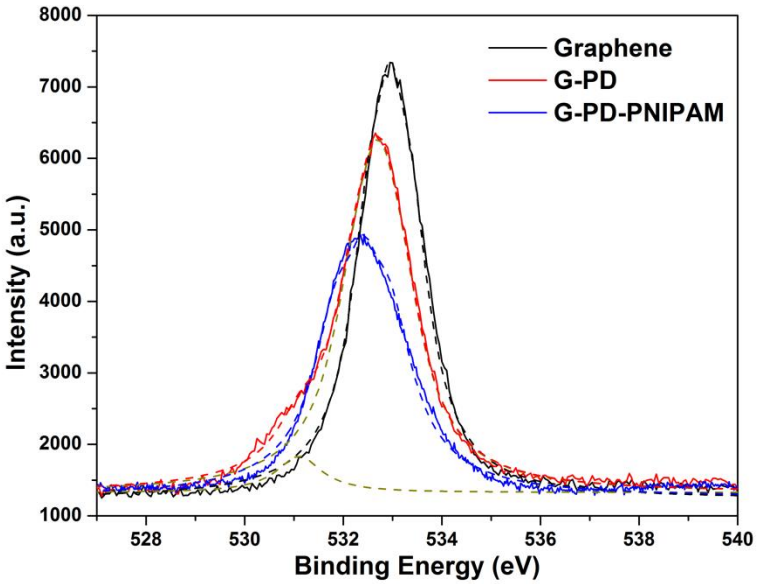

fig. S4. High-resolution O1s XPS spectra and peak fitting (dotted lines) of graphene, G-PD, and G-PD-PNIPAM.

Figure 2D shows the N1s high resolution spectrum. There is no peak exist for graphene because of the lack of the nitrogen element in graphene. For G-PD the peak can be deconvoluted and fitted with two peaks centering at 399.5 eV and 400.5 eV, which can be assigned to the primary amine and secondly amine , respectively, with the primary amine groups constituting the major contribution for polydopamine. The N1s peak for G-PD-PNIPAM has a much higher intensity, and can be fitted with one peak centering at 400.5 eV, because the grafted PNIPAM chains have higher nitrogen content and only secondary amine groups. The overall element ratio of graphene after polydopamine deposition and subsequent PNIPAM grafting changes significantly. For instance, the N:C:O ratio is 1: 18.1: 9.1 for G-PD, and 1: 7.0: 2.1 for G-PD-PNIPAM. All of the surface analysis data confirm the surface modification of graphene with PD and PNIPAM.

5. Optical and SEM imaging of the self-folding graphene structures

In the experiment, we placed a rigid SU-8 epoxy hinge in the center of the top two faces, in order to separate them and induce the folding of a closed box, in which the top face will be the lid. The length of the SU-8 hinge is the same as one side of the box (200 µm), the width of the hinge is 25 µm, and the thickness is around 300 nm. Since the width of the SU-8 hinge is small compared with the size of the face, it simply acts as a rigid hinge, and we found that variation of the hinge width does not significantly affect the extent of folding when it is thin. For instance, a box with the same materials and dimension, but with a SU-8 hinge of 12.5 µm wide show very similar folding behaviors as that of the original samples (25 µm wide hinge; Fig. 3, G to I in the main text), as shown in fig. S5 a to c. On the other hand, using coarse-grained molecular dynamics (MD) models, we found that when the hinge width becomes quite large (above 40 µm), it will affect the folding of the top two faces, as shown in fig S5 (d to f).

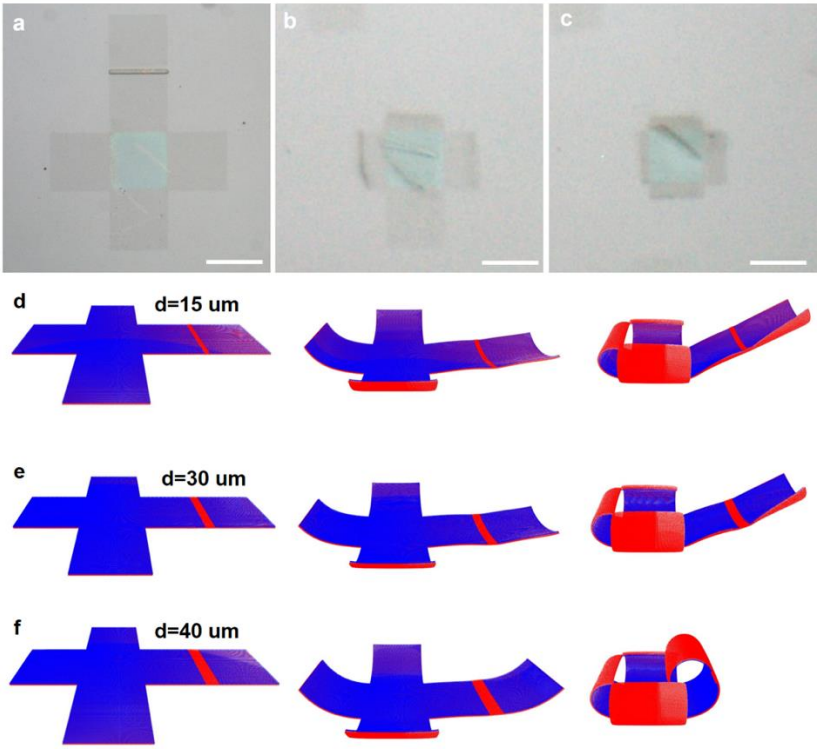

fig. S5. Effect of the rigid hinge on the self-folding of functionalized graphene box. (a to **c)** Self-folding process of a functionalized graphene box with a 12.5 µm wide hinge, panels a, b, c corresponds to the sample before, during and after folding, respectively. The scale bars are 200 µm. (**d** to **f**) The self-folding process of a graphene box with different hinge widths (15, 30 and 40 µm), obtained from coarse-grained MD model. When the hinge width is thin, the folding is not significantly affected but when the width increases the folding can be affected.

SEM images of the representative folded structure in the dry state are shown in fig. S6, it can be seen that the functionalized graphene microstructures are stable and uniform, and tend to collapse onto the substrate upon drying.

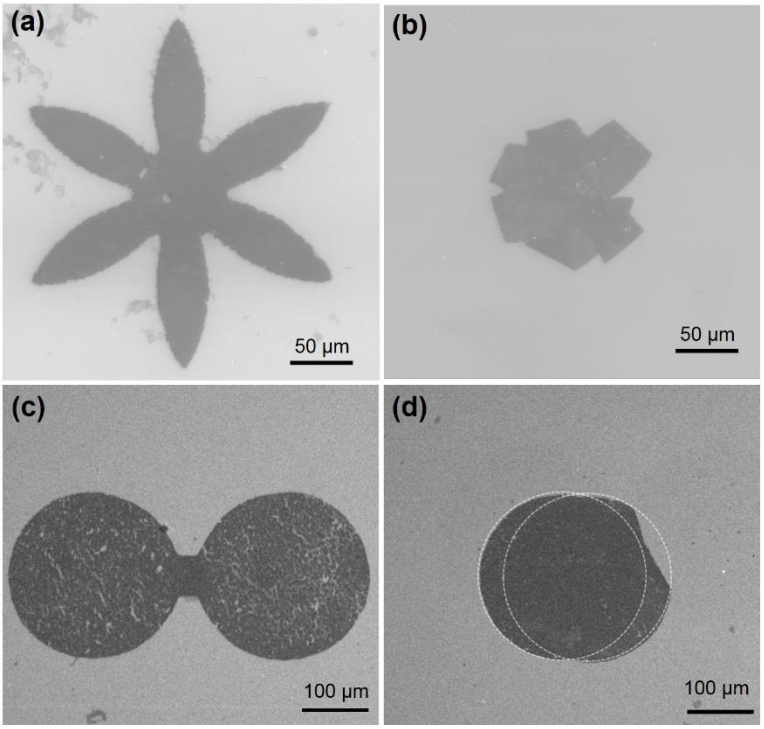

fig. S6. Characterization of the self-folding graphene microstructures using SEM. SEM images of the G-PD-PNIPAM flower (**a** and **b**) and dumbbell (**c** and **d**), before and after folding, the white circles in panel d represents the outlines of the two graphene disks in the dumbbell.

To show that the temperature induced self-folding process has high efficiency and high yield, optical images of a large area of the graphene flowers during folding are shown in fig. S7, which demonstrates the parallel and high throughput nature of our process. Moreover, to prove that the folding of the functionalized graphene is induced by PNIPAM chains contraction at elevated temperature, we also performed a controlled experiment with a patterned pristine graphene dumbbell and a G-PD dumbbell at the same condition, and both of the two samples do not show self-folding behavior at increased temperature due to the absence of PNIPAM brushes (fig. S8).

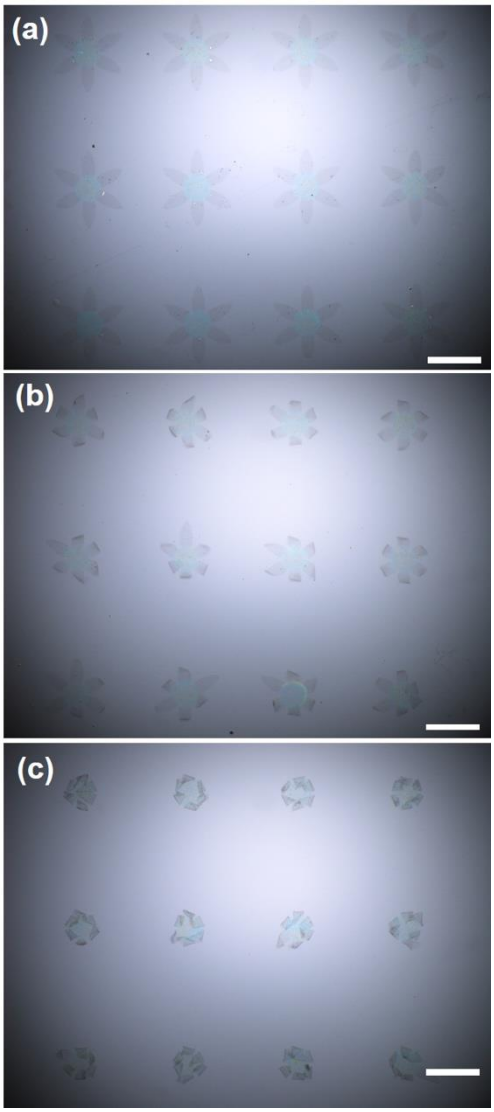

fig. S7. Highly parallel self-folding of ultrathin 3D graphene microstructures. Optical microscope images of a large area of graphene flowers before (**a**), during (**b**) and after (**c**) self-folding induced by temperature increase. Scale bars are 200 μm.

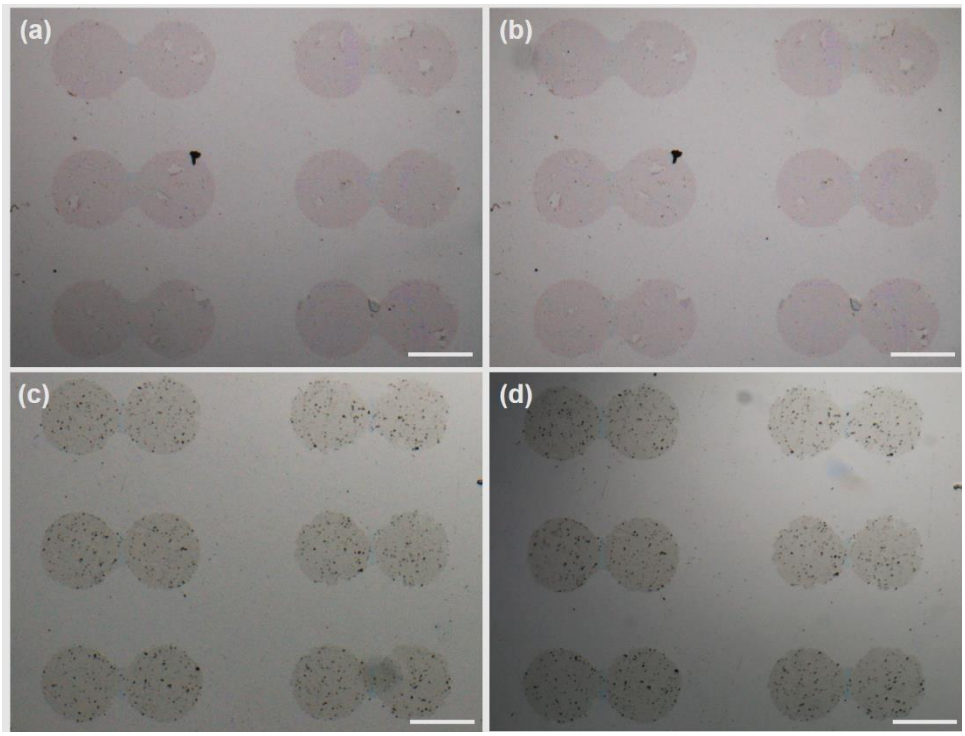

fig. S8. Control experiments of self-folding on pristine graphene and G-PD. Optical microscope images of pristine graphene dumbbells (**a** and **b**) and G-PD dumbbells (**c** and **d**) at room temperature (left column) and after heating to 45 °C (right column), both samples do not show self-folding behavior. Scale bars are 200 μm.

The thickness of the functionalized graphene can be further decreased by reducing the polymerization time of PD, as well as the grafting time of PNIPAM brushes. For instance, with a PD polymerization time of 1h, and PNIPAM grafting time of 3h, we are able to reduce the total thickness to 5 nm (fig. S9a). Moreover, the thinner functionalized graphene is still temperature responsive and self-folding can be achieved (fig. S9).

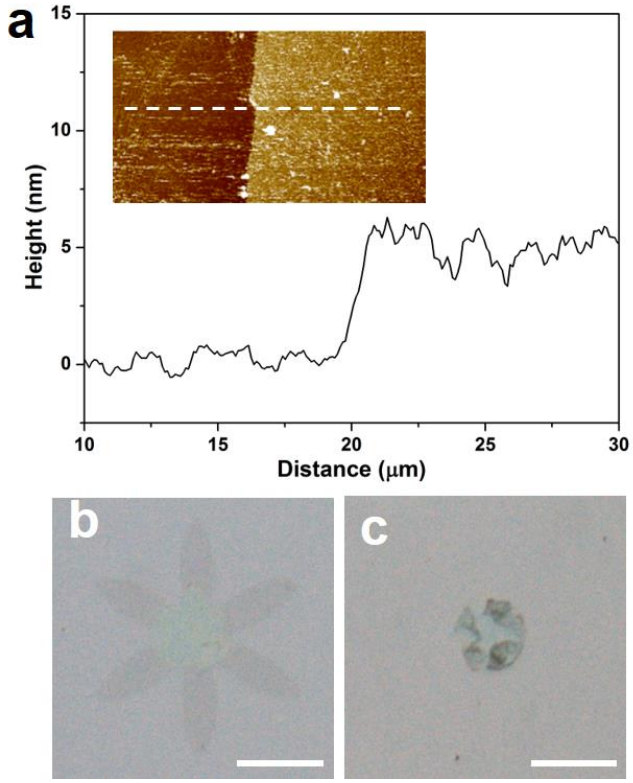

fig. S9. Self-folding of functionalized graphene with 5 nm thickness. (**a**) Thickness measurement of the G-PD-PNIPAM sample with reduced thickness, inset is the AFM height image. (**b** to **c**) Self-folding of the thin functionalized graphene flower with increasing temperature. Scale bars are 100 μm.

Temperature can be used to control the folding extent for simple and regular shaped functionalized graphene microstructures at certain temperature range. As shown in fig. S10, we studied the folding process of a half-functionalized graphene dumbbell, panel a is the original flat state, and panels b-f correspond to temperature of 35ºC, 38ºC, 41ºC, 43 ºC and 46 ºC, respectively. Within this temperature range, the higher the temperature, the higher the extent of folding can be achieved. But it needs to be noted that even higher temperature (above 45 ºC) does not have significant difference to the folding compared with that of 45 ºC, because it is already well above the LCST of PNIPAM.

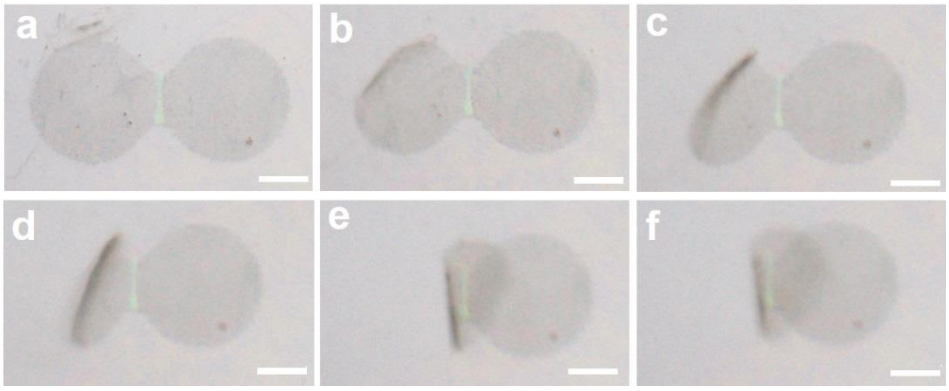

fig. S10. The folding process of half-functionalized graphene dumbbell with increasing temperature. From a–f the solution temperature is 25, 35, 38, 41, 43 and 46 ºC, respectively. All scale bars are 100 μm.

6. Raman spectra of folded graphene

In order to show that the graphene retains its molecular structure and high quality in the temperature induced folding process, Raman spectroscopy was used to characterize the folded microstructures. As shown in fig. S11, which is a folded graphene flower in the dry state, and Raman spectra were collected at two representative spots, one is in the unfolded monolayer region, and the other is in the folded bilayer region. It can be seen that Raman spectra of both spots have a sharp G and 2D band, with a weak D band. The intensity of both G band and 2D bands have an obvious increase for the folded region, and the I_{2D}/I_G ratio increases from 1.78 at the flat region to 2.27 at the folded bilayer region. Moreover, the position of the G and 2D band have almost no change before and after folding, which is quite different from previous reports on bilayer graphene when the two layers are in intimate contact (the 2D band of bilayer graphene is blue-shifted relative to monolayer graphene, with the blue-shift magnitude depending nonmonotonically on the rotation angle), the main reason is the PD and PNIPAM brushes in between the two graphene layers eliminate their strong interaction.

Moreover, the D band does not change for the folded region, which is quite different from previously reported folded graphene, and means the folding process does not induce additional defects, the interaction between the two graphene layers is screened by the thin polymer layer in between. When graphene folded directly on itself, there will be a second peak in the D band region, which has been called the I band. This is a nondispersive peak that arises from a weak but well-ordered perturbation caused by the folded layer upon the parent layer. In our case, due to the existence of a thin polymer layer in between the folded graphene, such a perturbation is largely eliminated, so the I band is not present here.

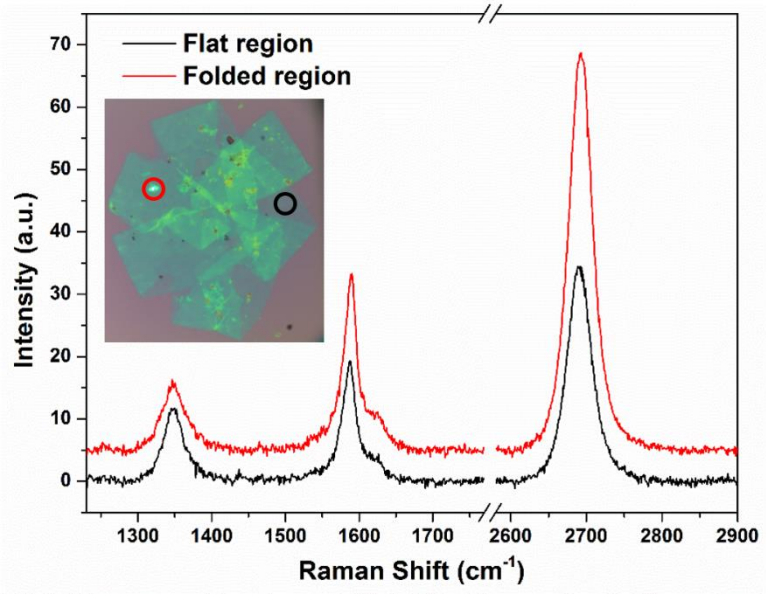

fig. S11. Raman spectra of a graphene flower in the flat and folded regions. The inset is the optical microscopy image taken with the Raman microscope. The black and red circles indicate flat and folded regions where the spectra were taken.

7. Cell encapsulation and Raman analysis

Self-folding graphene microstructures have promising biomedical applications due to their ultrathin nature, pliability and good biocompatibility. As an example, self-folding graphene flowers were used as soft grippers to encapsulate live cells. Pristine graphene itself is very hydrophobic, and the cell adhesion on it is not as good as bare glass substrate. As shown in fig. S12a, the cell density is lower on pristine graphene, but all the cells are alive on graphene, which indicates its good biocompatibility. On the other hand, after surface functionalization with PD and PNIPAM, which increases the hydrophilicity, the G-PD-PNIPAM shows increased cell density indicating excellent cell adhesion in addition to biocompatibility (fig. S12b).

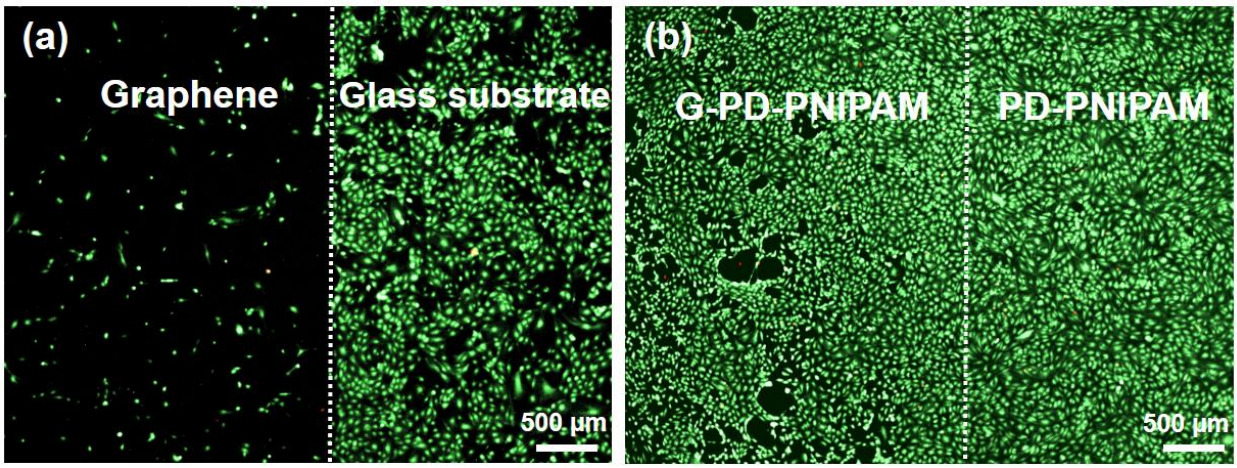

fig. S12. Cell viability with the live/dead assay. (**a**) Representative fluorescent image of the cells on graphene, live cells were stained green (calcein AM) while dead cells were stained red (ethidium homodimer). (**b**) Representative fluorescent image of the cells on functionalized graphene (G-PD-PNIPAM).

After encapsulation with the ultrathin graphene, we performed a Raman study on the encapsulated live cell, and the results showed that the Raman signals from the relevant biological molecules in the cell are significantly enhanced, which is useful for biosensing and biodetection. More specifically, as shown in fig. S13, for flat G-PD-PNIPAM, there are two main peaks, G and at 1590 cm^{-1}, and 2D band at 2638 cm^{-1}; as well as a weak D band at 1350 cm^{-1}. As a control, the folded functionalized graphene without cell inside show similar peaks, with an increase in G and 2D band intensity.

After encapsulation of the cell inside the functionalized graphene, there are pronounced changes and new peaks in the Raman spectrum. For instance, the $N^{+}(CH_3)_3$ symmetric stretch vibrations of the choline moiety at 711 cm^{-1} are observed. This is a characteristic peak for phospholipids, one of the major constituents of cellular membranes. The ring breathing modes in the DNA and RNA bases at 786 cm^{-1},

and the symmetric O-P-O stretching vibrations in RNA at 808 $cm^{-1}$are observed; both of which are located in the nuclei of the cells. The symmetric breathing mode of phenylalanine at 1003 cm^{-1}, which is a typical Raman feature for proteins is also present. The peak at 1450 cm^{-1} peak corresponds to CH_2 deformation from phospholipids and proteins. Moreover, there is a shoulder peak at 1610 cm^{-1}, which corresponds to phenylalanine, a major component of proteins. There is also a large increase in the G band and 2D band intensity, and the former is due to phenylalanine, the latter one comes from the different biomolecules (such as proteins) in the cell. The D band intensity also significantly increased after cell encapsulation, which indicates an intimate contact and interaction between graphene and the cell which induces some extent of structural changes and defects to graphene.

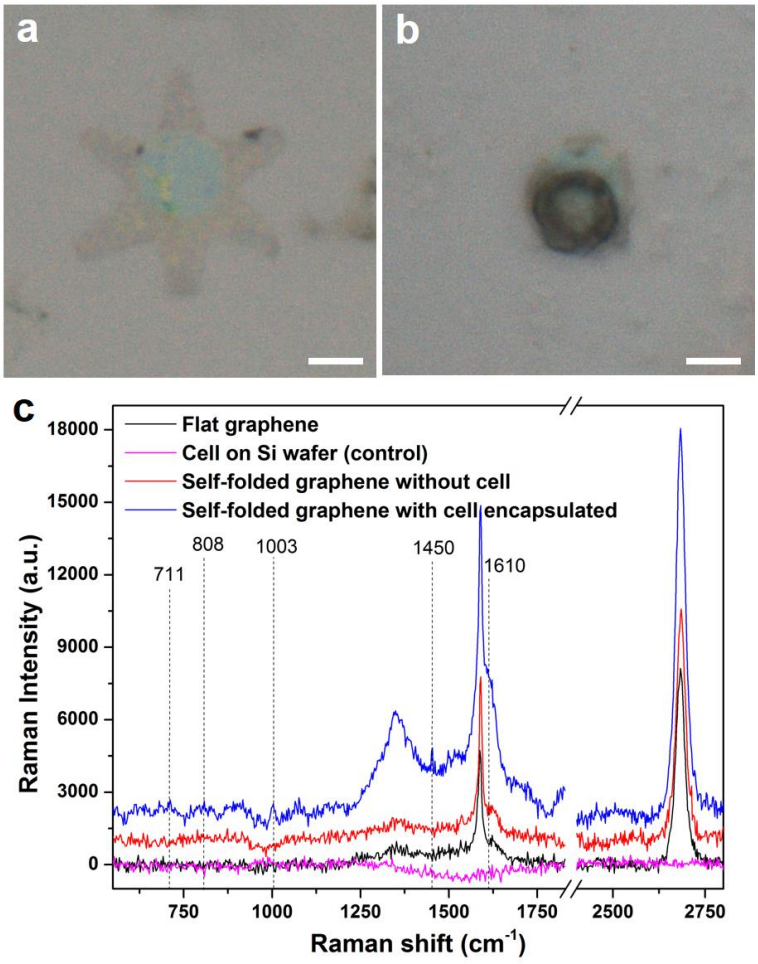

fig. S13. Single cell encapsulation and Raman study. A functionalized graphene flowers in flat state (**a**), and after encapsulation of a single breast cancer cell (**b**). (**c**) Raman spectra of functionalized graphene and after its encapsulation of a breast cancer cell. Scale bars are 10 µm.

8. Full atomistic modeling of the folding behaviors

Since both the PD and PNIPAM layers are very thin (i.e., 3~5 nm in the dry state), it is difficult to measure their mechanical properties experimentally with high accuracy, especially in an aqueous condition where the folding is conducted. We have carried out a full atomistic computational study on PNIPAM and PD using MD simulations (details in the Method part) to supplement our experimental work and provide the required coefficients for our coarse-grained MD model.

8.1. Estimation of PNIPAM's volume

PNIPAM always absorbs a certain amount of water, and thus the volume of PNIPAM includes the volume of the surrounding water. After the MD equilibration, the coordinates of the PNIPAM chains as well as the surrounding water molecules (within a cutoff of 5 Å) were used to estimate the volume of the PNIPAM aggregate in the system. The triangular surface plot in MATLAB was applied to generate a surface of the PNIPAM aggregate based on these coordinates. As the surface of the PNIPAM aggregate is defined, its volume can be calculated.

8.2. Estimation of PNIPAM's Young's modulus

After the MD equilibration, the extra water molecules (larger than a cutoff of 5 Å) were removed from the PNIPAM-water systems (i.e., at 275 K and 325 K), and the systems were then equilibrated with the NPT ensemble at a constant temperature of 275 K and 325 K for another 10 ns, respectively. The pressure was set to 1.013 bar in all three directions. The constrain at the bottom part of each PNIPAM chain was released to prevent obtaining unreasonable results from tensile tests, which were performed to estimate the modules of PNIPAM. A tensile stress of 10 MPa was applied to the PNIPAM-water systems (with extra water molecules removed) in the *y*- or *z*-directions and the corresponding tensile strain was measured with the NPT ensemble at a constant temperature of 275 K and 325 K for 1.0 ns, respectively. Except for the stretching direction, where the tensile stress was applied, the pressures in the other two directions were set to 1.013 bar. The Young's modulus of PNIPAM was estimated as the ratio of the applied tensile stress and corresponding tensile strain.

8.3. Coarse-grained modeling and equilibration

Each layer of the composite membrane material is modeled by an elastic network with carefully chosen elastic constants to match the materials' elastic properties and mass concentrated at the junction beads to match the material densities, such a strategy has been proven to be efficient to model other biological materials. It is noted that both the bond length and stiffness constant change only apply to the PNIPAM layer while these parameters for the graphene and PD layer are kept constant through the simulation.

We used the FCC lattice to model the location of the mass beads (which locate at corners and face centers) and used an elastic spring to model the interaction between the nearest neighboring beads. The total energy function is given by

$$E = E_T = \sum \varphi_T(r) \tag{1}$$

where E_T is the deformation energy for stretching/compression of all the springs. Each energy term was defined by

$$\varphi_T(r) = k(r - r_0)^2 \tag{2}$$

where 2*k* is the spring stiffness, $r_0 = a/\sqrt{2}$ is the equilibrium distance between two neighboring beads and a is the lattice constant of the FCC lattice. By assuming the polymers have Poisson ratio of ν=0.25, the Young's modulus *E* of such material composed of FCC lattice and elastic springs is given by

$$E = \frac{16k}{3a} \tag{3}$$

where *E* is the Young's modulus. The bending stiffness the PD layer of *l*=5 nm in thickness is given by $D = EI = E\frac{l^3}{12} = 52$ nN·nm, given the fact that the Young's modulus of PD material is *E*=5 GPa, which is obtained from the full atomistic MD simulations and experiments. It is noted that such stiffness is two orders of magnitude higher than the bending stiffness of a single layer of graphene as 0.15 nN·nm for a unit width of graphene and thus we do not explicitly model graphene in this coarse-grained model.

Considering the fact that the membrane is extremely thin as the two dimensions in the in-plane directions (>100 μm) are more than four orders of magnitudes larger than the membrane thickness (5 nm) and for the sake of simplicity of the numerical model and a smaller number of total coarse-grained beads. We scale up the thickness in the coarse-grained model to a length same as the lattice constant of *l*=*a* but scale down the *k* value to keep the bending stiffness to be the same for each layer. Therefore, we have

$$k\,(t) = \frac{9D(t)}{4a^2} \tag{4}$$

where *D* is the bending stiffness of each of the two layers, evolving as a function of time simply as $D(t) = D_{end} + (D_0 - D_{end})\exp(-\frac{t}{t_0})$, where D_0 is the bending stiffness at low temperature at beginning and D_{end} is the bending stiffness at high temperature, t_0 is a time constant with its numerical value of 2 s applied to all of our coarse-grained simulations. In the simulation of the coarse-grained model, we also

implicitly simulate the effect of the temperature on PNIPAM brushes layer by tuning the equilibrium length constant of the lattice structure as

$$a\,(t) = a_{end} + (a_0 - a_{end})\exp(-\frac{t}{t_0}) \quad (5)$$

where $a_0 = 4$ μm is the initial lattice length at low temperature, $a_{end} = 0.71a_0$ is the equilibrium length constant at high temperature, which reflects the 49% in-plane volume change for one length dimension, and t_0 is the time constant used in simulations to reflect how quick the PNIPAM responds to the temperature change.

8.4. Modeling of the folding behaviors

Since there is covalent bonding between PD and PNIPAM brushes, one end of the PNIPAM chains is fixed to the PD layer. To mimic this mechanical boundary condition, the bottom part of each PNIPAM chain is fixed in the x-direction (fig. S14). As a result, the bottom part of each PNIPAM chain cannot move in the x-direction but is free to move in the other two directions. The 12-6 Lennard-Jones interactions and Coulombic interactions were computed with a cutoff of 8 Å and 10 Å, respectively. The long-range interactions were calculated with a particle-particle particle-mesh solver (pppm). The integration time step was set to 1.0 fs.

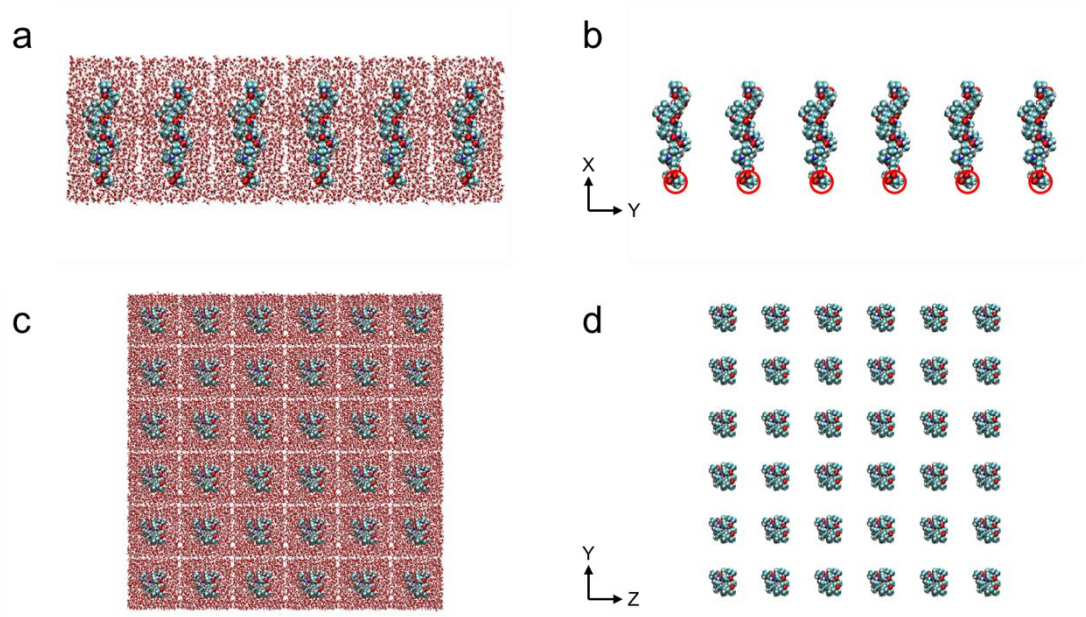

fig. S14. Initial configuration of the PNIPAM-water system in the MD model. The PNIPAM model consists of 36 PNIPAM chains with a chain length of 20-mer. The longitude direction of each PNIPAM chain is faced to the *x*-direction of the simulation box, and the PNIPAM chains are separated with a distance of 30 Å in both the *y*- and *z*-directions. The mass of the PNIPAM chains is around 10% of the mass of the water molecules. The initial configuration in the *x*-*y* direction is shown in (**a**) as well as (**b**), in which water is not shown for clarity. The initial configuration in the *y*-*z* direction is shown in (**c**) as well as (**d**), in which water is not shown for clarity. The red circles in (b) indicate the bottom part of each PNIPAM chain, which is fixed during the equilibration.

Figure S15a show the equilibrium structures of an array of 36 PNIPAM brushes at 275 K. When the temperature is lower than LCST, the PNIPAM chains are in the swollen hydrated state, which absorbs a large amount of water around the polymer chains. The volume of the PNIPAM aggregate was calculated as the sum of the volume of the PNIPAM chains and the volume of the surrounding water. The surface of the PNIPAM aggregate is shown in fig. S15b and the volume is around 308 nm^3. On the other hand, when the temperature is higher than LCST, the PNIPAM chains are in the shrunken dehydrated state, which are mostly hydrophobic. Fig. S15c show the equilibrium structures of the PNIPAM brushes at 325 K and the surface of the PNIPAM aggregate is shown in fig. S15d. Due to the fact that a large amount of water is lost at 325 K, the volume of the PNIPAM aggregate is decreased to around 157 nm^3, which is only 51% of the volume at 275 K.

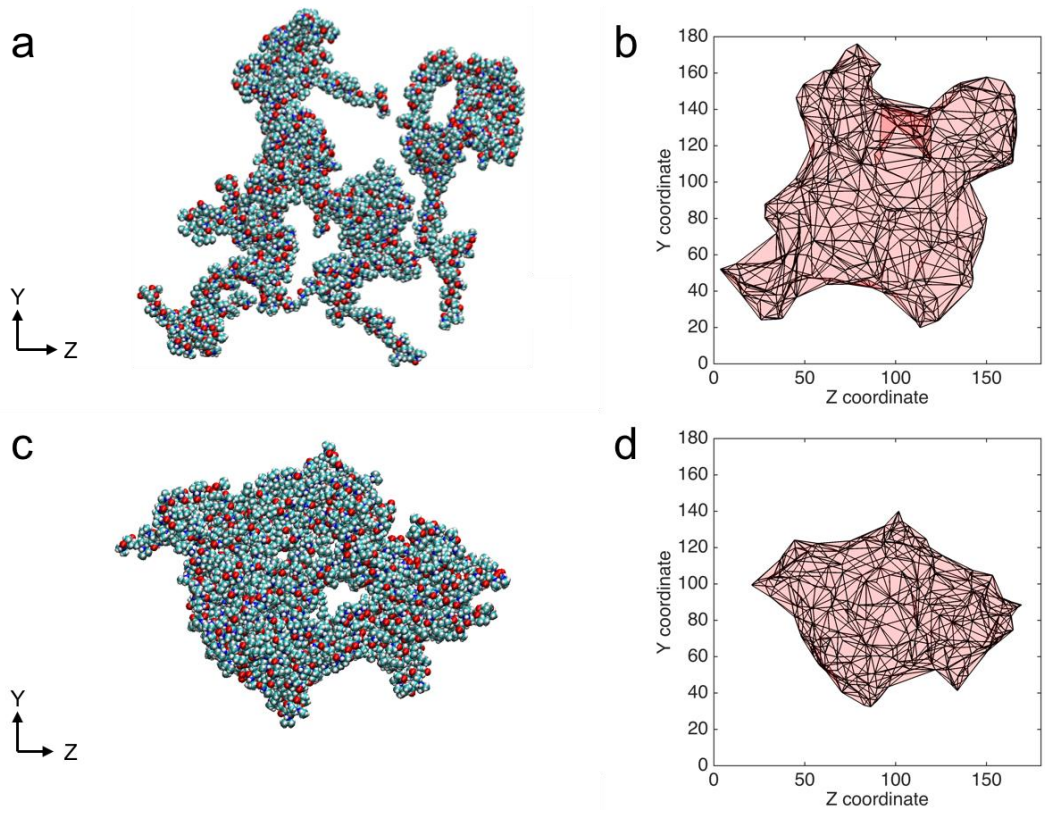

fig. S15. Top view of the aggregation behavior of an array of (36 chains in total) PNIPAM brushes at different temperatures in MD simulations. (**a**) The equilibrium structure of PNIPAN brushes at 275 K and (**b**) the surface of the aggregate. (**c**) The equilibrium structure of PNIPAN brushes at 325 K and (**d**) the surface of the aggregate. Water is not shown in (a) and (c) for clarity.

In this study, tensile tests were performed to estimate the Young's modulus of PNIPAM. The tensile test results are shown in table S2. Since the self-folding mechanism of the graphene microstructures is caused by the in-plane (*y*- and *z*- directions) stresses of PNIPAM, only the in-plane Young's moduli are calculated. At a temperature of 275 K, the Young's moduli of PNIPAM are calculated as 87 MPa and 101 MPa in the *y*- and *z*- directions, respectively, resulting in an average of ~94 MPa. On the other hand, at a temperature of 325 K, the Young's moduli of PNIPAM are calculated as 221 MPa and 265 MPa in the *y*- and *z*- directions, respectively, resulting in an average of ~243 MPa. As the temperature difference is only 50 K, which has a negligible effect on the intrinsic Young's modulus, the difference between the Young's moduli at different temperatures is mainly caused by the structural transformation of the PNIPAM chains.

table S2. Tensile test results of PNIPAM from the MD simulations. The Young's moduli of PNIPAM is calculated as ~94 MPa and ~234 MPa at 275 K and 325 K, respectively.

System	L_X (Å)	L_Y (Å)	L_Z (Å)	S_{XX} (MPa)	S_{YY} (MPa)	S_{ZZ} (MPa)	E (MPa)
275 K (eq)	37.0	96.2	85.5	-0.1	-0.1	-0.1	N.A.
275 K (Y)	36.0	107.2	79.2	-0.1	10	-0.1	87
275 K (Z)	35.9	90.3	94.0	-0.1	-0.1	10	101
325 K (eq)	27.8	86.0	103.4	-0.1	-0.1	-0.1	N.A.
325 K (Y)	27.3	89.9	101.3	-0.1	10	-0.1	221
325 K (Z)	27.1	85.6	107.3	-0.1	-0.1	10	265

We did a quantitative comparison between the coarse-grained model and the experiment results. For instance, for the self-folding graphene flower, the average lateral size and height in the folded state measured by confocal microscopy was found to be 131 (±14) and 58 (±17) μm (Fig. 3C), and those values are 125 and 52 μm (Fig. 5C) in the simulation. For the graphene box, the size in the folded state is 326 μm, and in the simulation it is 340 μm. Those data demonstrate that the coarse-grained models are accurate representations of the experimental structures.

In addition, we also studied the effect of the overall size (or size/thickness ratio) on the self-folding behaviors. As shown in fig. S16, smaller flowers (120 and 300 μm) have more regular and well-defined folding morphology, while for larger ones (600 μm), the petals tend to twist or wrinkle during the folding process. The main reason is that for the large flowers, the initial folding direction can be either along the long axis, or in the middle between the long and short axis, and its initially curved structure increases the bending stiffness in the orthogonal direction and prevents folding in that direction. The interplay between initial folding direction and the energy release during the membrane bending determines the final folding structure.

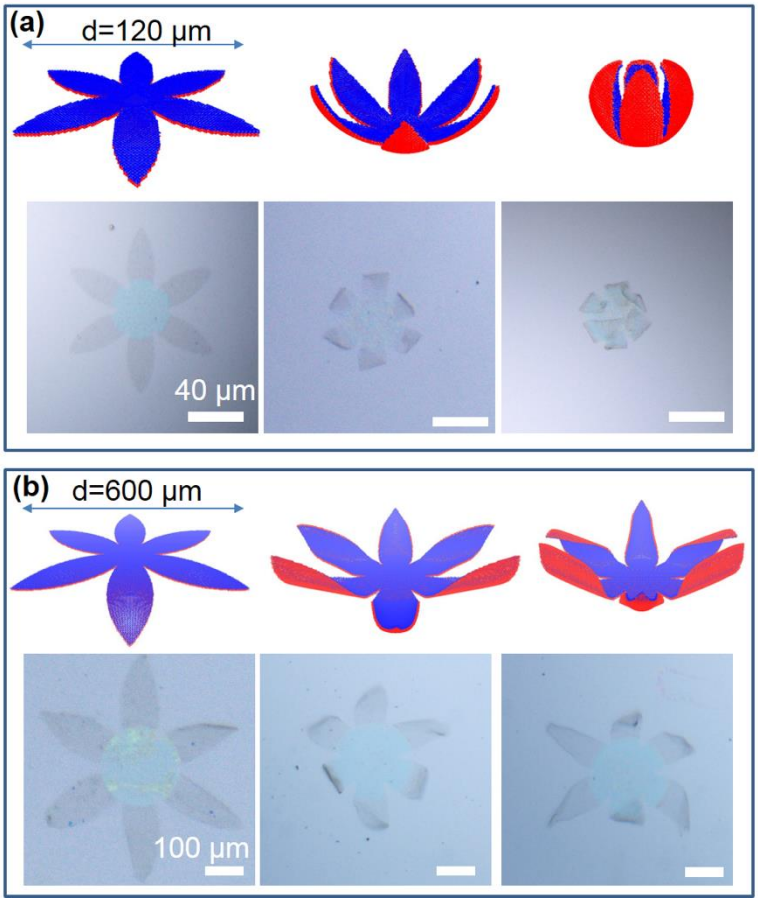

fig. S16. Comparison between the coarse-grained MD model and the experiment results for a functionalized graphene flower with different size. Panel (**a**) represents a flower with *d*=120 μm overall size of the initial pattern, and panel (**b**) is a *d*=600 μm flower.

Using this model, we can also design other material systems with different deforming ratio and material stiffness, which will play the main role in governing the resulting structure shape as shown in fig. S17. We can also change the fixed boundary condition and distribution pattern of the PNIPAM layer to result in different folded geometries.

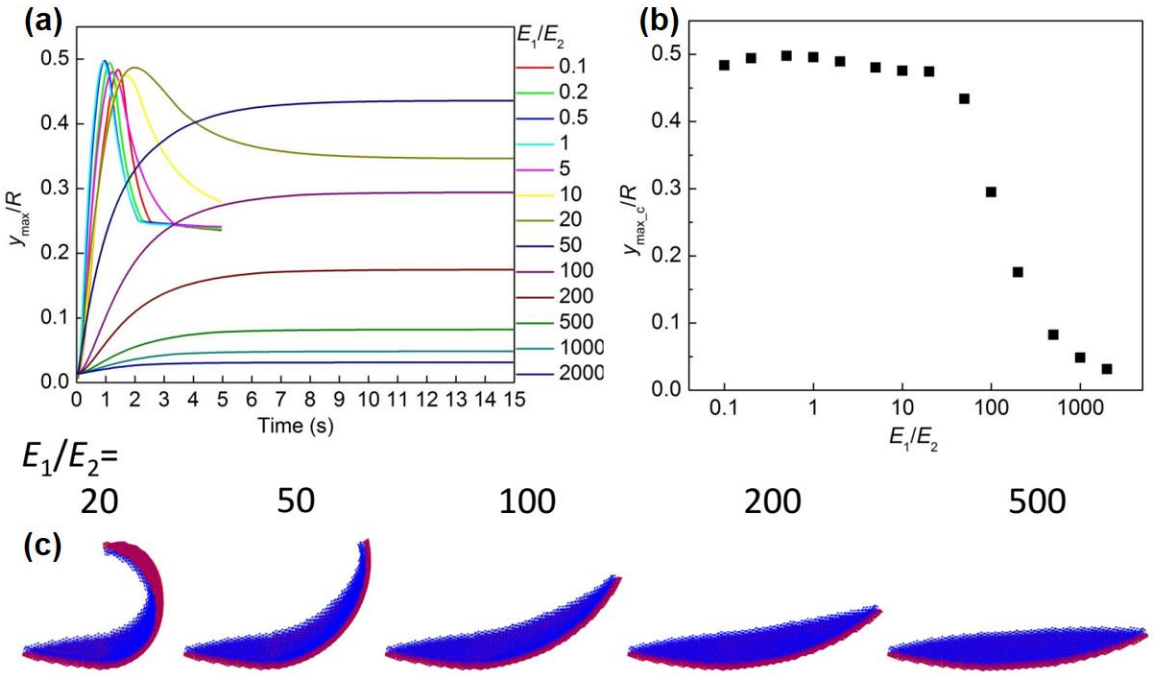

fig. S17. The effect of mechanical properties of the two layers on self-folding. The effect of the modulus ratio between the top (E_2) and bottom (E_1) layer on their folding behavior. (**a**) The maximum height (y_{max}) of the folded structure versus the overall radius (R) of the flower as a function of time. (**b**) The maximum height (y_{max_c}) of the folded structure versus the overall radius (R) of the flower as a function of the modulus ratio. (**c**) Simulation snapshots of the folded petals with different modulus ratio.

9. Electrical properties of folded graphene structures

The conductivity of the functionalized graphene microstructures was measured by the four-point probe method. The gold pads were placed directly on the graphene before it was functionalized with PD and PNIPAM. The functionalized graphene in the flat state has almost the same sheet resistance compared with that of pristine CVD graphene (fig. S18a).

As discussed in the main text, the folding crease can effectively alter the electrical property of functionalized graphene. In order to show that such a change is general and reproducible, we also conducted the same measurements on a graphene dumbbell with a different width of the folding crease, which is 20 μm, and other parameters are kept the same. The four-point probe measurement results are shown in fig. S18b, the general trend is the same with the dumbbell of 10 μm folding crease. The I-V curve becomes nonlinear after folding with a significant increase in resistance: 838 Ω before folding, and ranging from 1252 to1394 Ω after folding. The resistance of the folded dumbbell also has the maximum value around 0 V.

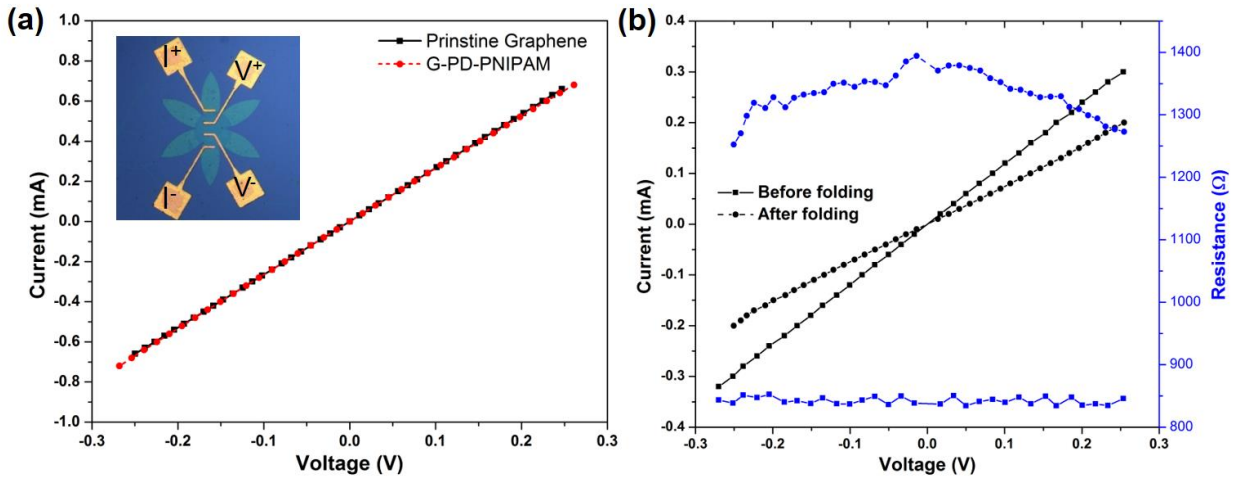

fig. S18. Electrical measurements on pristine graphene and functionalized graphene dumbbell. (**a**) I-V curves of the CVD graphene before and after surface functionalization, the inset is optical image of the 4-point probe device. (**b**) I-V curves and R-V curves of graphene dumbbell (with 20 μm wide center part) before and after folding.

The G-PD-PNIPAM has a total thickness of 8.9 nm in this study, so that when it folds on top of each other, a folding crease is formed at the edge, as shown in fig. S19. The SU-8 covered region is relatively far from the folding crease, so it does not have a significant effect on the crease formation. The height or diameter of the folding crease is measured by AFM, around 18 nm, which is quite small, but still much larger than that of a carbon nanotube, so that mechanical fracture of the graphene is unlikely to happen.

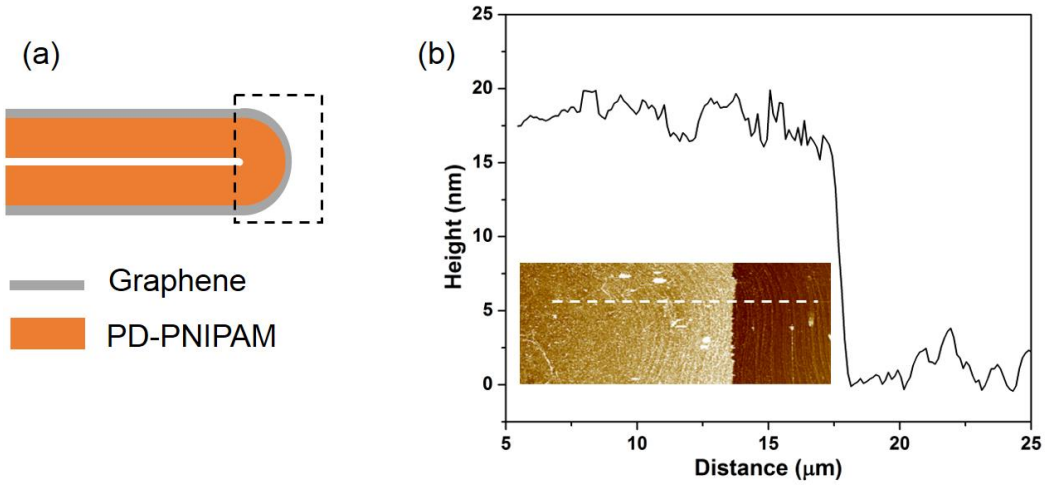

fig. S19. Dimension of the folding crease measured by AFM. (**a**) Schematic representation of the folding crease region, which is marked with a dash line box. (**b**) The height or diameter of the folding crease as measured by AFM cross-section analysis.

Figure S20a shows the output characteristics (I_d vs V_d) of the graphene FET on a 300 nm SiO_2 dielectric at different V_g (gate voltage). The channel width and length are 125 and 230 μm, respectively. The curve shows a perfect linear behavior and a decrease in conductance when the gate voltage changes from negative to positive values, which is typical for metal/graphene junctions. The transfer characteristics of the functionalized graphene FET is shown in fig. S20b. It can be seen that the Dirac current (I_d) gradually decreases with increasing V_g, and the Dirac point is approximately + 90 V, which indicates that the graphene is heavily p-doped, and the probable reason is the adsorption of water molecules from air and polymer residue from the transfer process. The output curves of the functionalized graphene FET are shown in fig. S20c. The behavior is similar to that of the pristine graphene FET, and proves that the non-covalent functionalization does not change the intrinsic electrical properties of graphene.

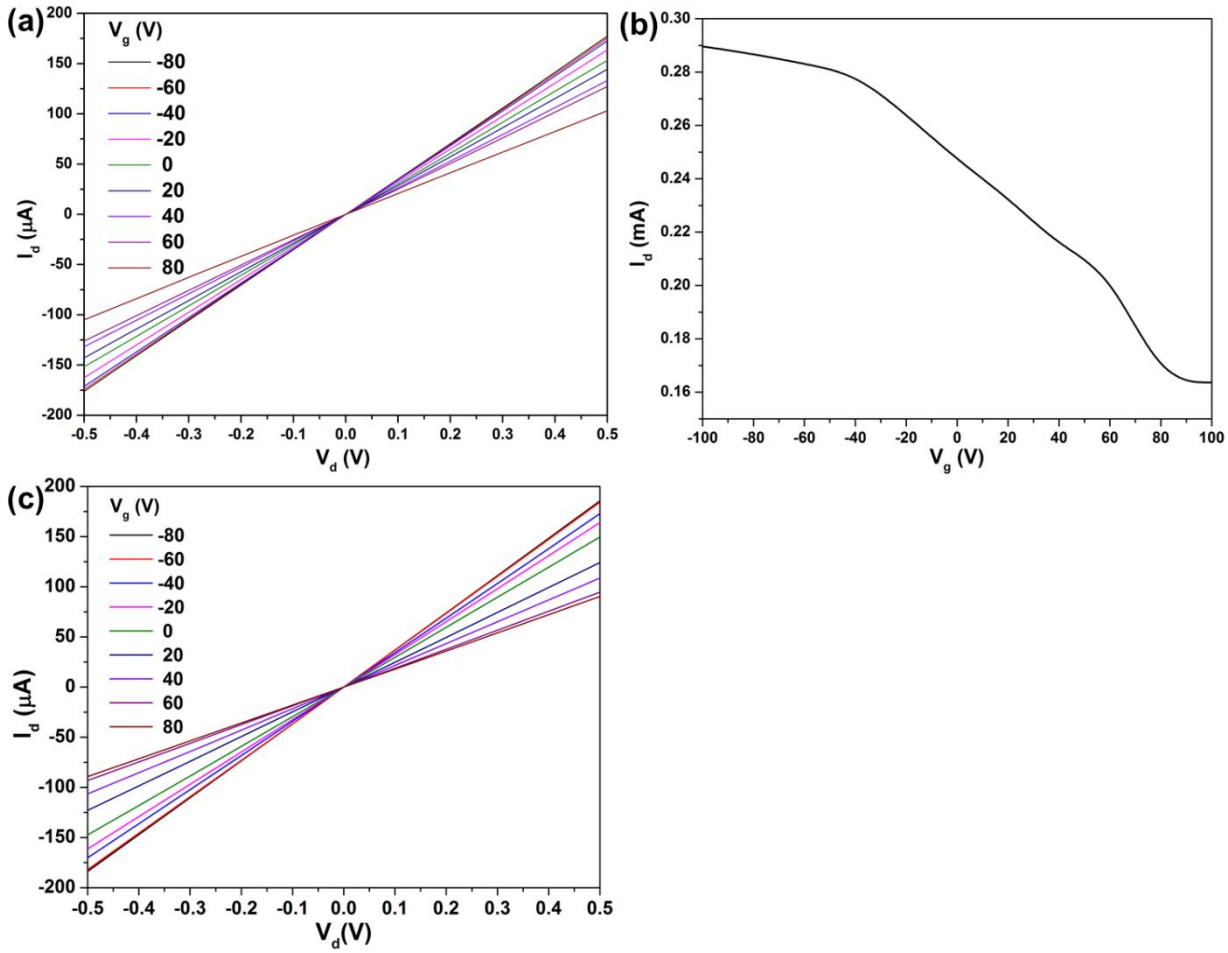

fig. S20. Output and transfer curves of the pristine and functionalized graphene FET. (**a**) Output curves of the pristine graphene FET as a function of bias with varying gate voltages. (**b**) Transfer curve of the pristine graphene FET as a function of back gate voltage. (**c**) Output curves of the functionalized graphene FET as a function of bias with varying gate voltages.